Improvement of Electrochemical Stability using the Eutectic Composition of a Ternary Molten Salt System for Highly Concentrated Electrolyte for Na-ion Batteries

Jinkwang Hwang,[a] *Ashvini Nair Sivasengaran*,[a] *Huan Yang*,[a] *Hiroki Yamamoto*,[a] *Takashi Takeuchi*,[a] *Kazuhiko Matsumoto*,[*,a,b] *Rika Hagiwara*[a,b]

[a]Graduate School of Energy Science, Kyoto University, Yoshida-honmachi, Sakyo-ku, Kyoto 606-8501, Japan

[b]Unit of Elements Strategy Initiative for Catalysts & Batteries (ESICB), Kyoto University, Katsura, Kyoto 615-8510, Japan

*Corresponding Author

E-mail: k-matsumoto@energy.kyoto-u.ac.jp

ABSTRACT

The increase in the concentration of electrolytes for secondary batteries has significant advantages in terms of physicochemical and electrochemical performance. This study aims to explore the highly concentrated electrolyte for Na-ion batteries using a ternary salt system. The eutectic composition of $Na[N(SO_2F)_2]$–$Na[N(SO_2F)(SO_2CF_3)]$–$Na[SO_3CF_3]$ ternary molten salt system increases solubility into an organic solvent, enabling the use of highly concentrated electrolytes for Na-ion batteries. The ternary salt system achieved concentrations of 5.0 m (m = mol kg^{-1}) with propylene carbonate (PC), 2.9 m with dimethoxyethane, 2.0 m with ethylene carbonate/dimethyl carbonate, and 3.9 m with ethylene carbonate/diethyl carbonate. The highly concentrated electrolyte of 5.0 m in PC suppressed Al corrosion and exhibited better oxidative stability. Stable electrochemical performance using a hard carbon/$NaCrO_2$ in full cell configuration introduces a new strategy to explore highly concentrated electrolytes for secondary batteries.

Keywords: sodium-ion batteries, electrolytes, molten salt, highly concentrated electrolytes, hard carbon, $NaCrO_2$

1. INTRODUCTION

Electrochemical energy storage requires different kinds of batteries, which function to mutually convert chemical energy and electrical energy within an electrochemically active material through redox reactions.[1] Batteries can mainly be classified into primary and secondary batteries, the former being able to be used only once, whereas the latter allows repeated charging and discharging mechanisms making them more suitable for various applications.[2-3] There is a number of variations in the secondary batteries, such as nickel-hydrogen, lead-acid, and as well as lithium-ion batteries (LIBs).

In particular, LIBs have gained popularity in recent decades due to their suitability for application in mobile and portable devices because of their high energy densities, which allow the design smaller than other types of batteries.[3-4] Despite their various advantages, the LIBs also have certain drawbacks that have urged us to find alternatives. The scarce and uneven distribution of lithium resources could lead to political interference that results in the monopoly and the unpredictable price of lithium resources, whereas sodium resources are evenly distributed, making sodium-ion batteries (SIBs) easily accessible throughout the globe.[3-6] This, in turn, contributes to a significant difference in the price of raw material, which contributes to the overall feasibility of batteries leaning towards SIBs as prospective replacements for some applications.[5-8]

The majority of Na-ion batteries previously reported utilizing organic solvents with moderate concentrations (~1 mol dm^{-3}) of Na salts.[9] However, the scarcity of electrolytes capable of producing robust solid-electrolyte interphases (SEIs) has substantially impeded their technological advancement.[10-12] Nonetheless, as the need for safety and high performance outweighs concerns of deploying new electrolytes,[9,13-14] such as highly concentrated electrolytes have gained traction in both nonaqueous and aqueous systems.[7] Recent reports on nonaqueous and

aqueous highly concentrated electrolytes demonstrated remarkable performance on electrodes and found to provide wide electrochemical windows, enhancing electrochemical stabilities in Li, Na, and K-ion batteries.[14-32] Thus, various combinations of salts and solvents have been attempted to achieve highly concentrated electrolytes.

Herein, we report a facile approach to developing highly concentrated electrolytes for SIBs using fundamental concepts of molten salt chemistry. Molten salts have been used as electrolytes for various electrochemical systems, including batteries in their history, and multiary salt systems are typically explored to decrease the melting point. Differential scanning calorimetry is conducted to determine the melting points for binary and ternary salt systems made from (Na[FSA]: sodium bis(fluorosulfonyl)amide), Na[OTf]: sodium trifluoromethylsulfonate, and Na[FTA]: sodium fluorosulfonyl) (trifluoromethylsulfonyl)amide (**Figures S1** and **S2**). Binary salt systems based on Na[FSA]-Na[OTf] and Na[FSA]-Na[FTA] with varied component ratios manifested melting points of around 370 K. As for the Na[FSA]-Na[FTA]-Na[OTf] ternary salt systems, low melting points are achieved in all the investigated ratios (Figure S2). Therefore, the Na[FSA] : Na[FTA] : Na[OTf] = 8 : 1 : 1 in mol (hereafter, Na[FSA][FTA][OTf]), which contains Na[FSA] in a relatively high composition, is representatively chosen because the high electrochemical performance of Na[FSA] is widely known in previous studies and the ternary system based on Na[FSA] (high Na[FSA] composition) is considered to be beneficial for battery performance. The neat Na[FSA][FTA][OTf] molten salt at 363 K exhibit high electrochemical stability on Pt and Al working electrodes, which implies this system is potentially useful as an electrolyte for SIBs (**Figure S3a**). However, the high melting point, high viscosity, and large bulk resistance of the molten salt system limited its practical use (see Figure 3b for the Nyquist plots of the Na/Na symmetric cell with this molten salt electrolyte), and the use of a solution based on this eutectic

system is more attractive for room-temperature application. Therefore, its solubility in propylene carbonate (PC), dimethoxyethane (DME), ethylene carbonate/dimethyl carbonate (EC/DMC), and ethylene carbonate/diethyl carbonate (EC/DEC) are examined, and the electrochemical performance of PC-based electrolyte is investigated with the hard carbon and $NaCrO_2$ as typical negative and positive electrode materials, respectively.[33-36]

2. EXPERIMENTAL SECTION

2.1 Materials and Handling All the non-volatile materials were handled under a dry Ar atmosphere in a glove box (H_2O < 1 ppm and O_2 <1 ppm). The salts, Na[FSA] (Mitsubishi Materials Electronic Chemicals, purity > 99%), Na[OTf] (Sigma-Aldrich, purity > 98%), and Na[FTA] (PROVISCO CS, purity > 98%) were dried under vacuum for 24 h at 363 K. The solvents, PC (Kishida Chemical), EC/DMC (1:1 v/v) (Kishida Chemical), EC/DEC (1:1 v/v) (Kishida Chemical), and DME (AccuStandard) were used without further purification. The typical water contents of the organic solutions were below 20 ppm according to Karl-Fischer titration (899 Coulometer, Metrohm).

2.2 Preparation of Electrodes. A slurry was prepared by mixing Hard carbon (HC) powder (CARBOTRON P, Kureha Battery Materials Japan Co., Ltd.), carbon black, and polyvinylidene difluoride (PVDF) (85:10:5 wt%) in *N*-methylpyrrolidone using a planetary mixer (AR-100, Thinky, Tokyo, Japan) and pasting the mixture on Al foil. $NaCrO_2$ was prepared by the solid-state method, as described in the previous study.[37] The prepared $NaCrO_2$ powder, carbon black, and PVDF (75:15:10 wt%) were well-mixed in *N*-methylpyrrolidone using the planetary mixer, and

the resulting slurry was pasted on Al foil. The electrodes were dried under vacuum at 353 K for 12 h.

2.3 Physical Characterization. Phase transition temperatures were determined by differential scanning calorimetry (DSC) (DSC-8230 Thermo Plus EVO II Series, Rigaku Corp.) at a scan rate of 5 K min^{-1} under a dry Ar atmosphere. The ionic conductivity was measured by an AC impedance technique using a 3532-80 impedance analyzer (Hioki E.E. Corp.). The electrolytes were loaded in a T-shaped poly(tetrafluoroethylene) cell with two stainless steel blocking electrodes in the glove box and placed in a temperature-controlled thermostatic chamber (SU-242, ESPEC). Viscosities were measured with an electromagnetically spinning viscometer (EMS-100, Kyoto Electronics Manufacturing Co., Ltd.). Densities were measured by a density meter (DMA 4500M Anton Paar). The electrolytes for density measurements were filled in a 1 mL syringe (Terumo SS-01T) with a rubber cap in a glove box and inserted into the density meter. The analyses were conducted in the temperature range from 293 to 363 K, with an increment of 5 K per minute.

2.4 Electrochemical Measurements. The weight ratio of active materials in the positive and negative electrodes was adjusted to 3.0 : 1.0, which corresponds to the capacity ratio of 1.2 : 1.0 = $Q_{\text{Positive electrode}}$: $Q_{\text{Negative electrode}}$ (Q denotes practical capacity) considering the practical capacities of $NaCrO_2$ (100 mAh g^{-1}) and HC (250 mAh g^{-1}). The loading masses of the positive and negative electrodes were 4.5-5 and 1.3-1.5 mg cm^{-2}, respectively. Galvanostatic charge-discharge tests were conducted using a three-electrode cell configuration (EC Frontier co., LTD) by separately monitoring the positive and negative electrode potentials. Sodium metal (Sigma-Aldrich Chemistry, 99.95% purity) was cut into a disk (13 mm diameter) and fixed on an Al plate current

collector as the negative electrode for half-cell measurement. Glass microfiber (Whatman GF/D) was used as a separator, and Na metal ring was used for a reference electrode. Cyclic voltammetry (CV) was carried out using a coin-cell configuration with an Al working electrode (10 mm diameter) and a Na metal counter electrode. Linear sweep voltammetry (LSV) was performed to 5.5 V with a Pt working electrode (10 mm diameter) and a Na metal counter electrode. Charge-discharge and CV tests were controlled by a VSP potentiostat (Bio-Logic) at 298 K.

2.5 Electrode and Electrolyte Characterizations. The symmetric cells for electrochemical impedance spectroscopy (EIS) were prepared using the electrodes after the charge-discharge test (SOC 30%). The full cells of HC/$NaCrO_2$ were disassembled, and each electrode was assembled as a symmetric cell of HC/HC and $NaCrO_2$/$NaCrO_2$ under dry Ar atmosphere in the glove box. The SEI layer components on HC were analyzed using X-ray photoelectron spectroscopy (XPS) (JEOL, JPS-9030, Mg *K*α source). The electrodes after electrochemical tests were washed with PC and dried under vacuum. Raman spectra were recorded on a Raman instrument (Thermo scientific, DXR3) using the 532 nm excitation line of diode-pumped solid-state laser.

3. RESULT AND DISCUSSION

In PC, solubilities of 2.5 m, 1.9 m, and 1.2 m were obtained from Na[FSA], Na[FTA], and Na[OTf], respectively, whereas the Na[FSA][FTA][OTf] system, achieved 5.0 m in the same solvent. Further solubility tests in other solvents EC/DMC and EC/DEC revealed very high concentrations of the Na[FSA][FTA][OTf] system, but a single Na[FSA] salt shows a higher solubility than the Na[FSA][FTA][OTf] system in DME probably due to the low solubility of Na[OTf] into DME (Table S1**)**.[30]

Higher solubility with the Na[FSA][FTA][OTf] system can be understood by considering the thermochemical cycle; the melting temperature of the ternary salt at the eutectic composition significantly decreases compared to those of the single salts owing to the Gibbs energy of mixing, which also leads to the additional stabilization energy in the solution state even other factors of the component salt contribute to the thermochemical cycle in the same manner as those of the single salts.

The Na[FSA][FTA][OTf]-PC system was selected for further examination since it exhibited the highest salt/solvent molar ratio (1/2.0 for 5.0 m) (Table S1). Temperature dependence of ionic conductivity and viscosity for the Na[FSA][FTA][OTf]-PC systems were fitted by the Vogel-Tammann-Fulcher (VTF) equations based on Eqs. 1 and 2:[38]

$$\eta(T) = A_\eta T^{1/2} \exp\left(\frac{B_\eta}{T - T_{0\eta}}\right) \qquad (1)$$

$$\sigma(T) = A_\sigma T^{-1/2} \exp\left(-\frac{B_\sigma}{T - T_{0\sigma}}\right) \qquad (2)$$

where $\eta(T)$ and $\sigma(T)$ are viscosity and ionic conductivity, respectively, A_η and A_σ refer to constants related to the values at infinite temperature, B_η and B_σ are constants related to the activation energy, and $T_{0\eta}$ and $T_{0\sigma}$ are ideal glass-transition temperatures. The VTF equation (**Eqs. 1** and **2**), typically applied in fragile systems,[39] was used to fit the Arrhenius plots of ionic conductivity and viscosity **(Figure 1a,b)** with summaries provided in **Tables S2** and **S3** (see **Figure S4** and **Tables S4** and **S5** for ionic conductivities and viscosities of the single-salt PC solutions). The ternary salts system shows higher ionic conductivities than the single-salt system at the same concentration.[40] At 293 K, ionic conductivities increase from 2.68 mS cm^{-1} (0.1 m Na[FSA][FTA][OTf]-PC) to 6.80 mS cm^{-1} (1.0 m Na[FSA][FTA][OTf]-PC) but decrease to 3.88 mS cm^{-1} (2.5 m Na[FSA][FTA][OTf]-PC), and 1.63 mS cm^{-1} (5.0 m Na[FSA][FTA][OTf]-PC), conforming to the typical concentration

dependency of ionic conductivity elucidated by several theoretical concepts such as the cubic root rule.[41]

The prepared electrolytes were also subjected to density tests in the temperature range from 293 to 363 K. The resulting density data are presented in **Figure 1c** for the Na[FSA][FTA][OTf]-PC systems (see **Figures S5**, Supporting Information, for the densities of single salt-PC). The density data were fitted with Eq. 3 with the fitting parameters *A* and *B*:

$$\rho = AT + B \quad (3)$$

The results of density are summarized in **Tables S6** and **S7** for the Na[FSA][FTA][OTf]-PC, and single salt-PC systems, respectively. The densities of the single salt-PC, as well as the Na[FSA][FTA][OTf]-PC systems, increase with an increase in molality and decrease with an increase in temperature. (See **Table S8**, Supporting Information for the molar concentration (mol dm^{-3}) of the Na[FSA][FTA][OTf]-PC systems)

Molar conductivity (λ) for the Na[FSA][FTA][OTf]-PC is calculated from the ionic conductivity and molar concentration (**Table S9**). The molar conductivity also shows temperature dependency, and the 0.1 m Na[FSA][FTA][OTf]-PC shows the highest molar conductivity in all the temperature ranges. Further analysis is carried out to investigate the concentration effect on the correlation between molar conductivity and viscosity, as expressed by Eq. 4, so-called the Walden rule.[22] The Walden rule is validated when the product of molar conductivity and viscosity is constant. **Figure S6** shows the Walden plots using logarithmic molar conductivity vs. logarithmic reciprocal viscosity of the Na[FSA][FTA][OTf]-PC systems. The dashed line indicates the visual guide based on 1 M KCl aqueous solution representing $\alpha = 1$ in Eq. 4. The Na[FSA][FTA][OTf]-PC systems and single salt-PC have a non-unity gradient in the Walden plot, which can be interpreted by the fractional Walden rule by Eq. 5:[42-44]

$$\lambda\eta = C \qquad (4)$$

$$\lambda\eta^{\alpha} = C' \qquad (5)$$

where C and C' are constants. **Table S10** lists the α and C' values which correspond to the gradient and vertical intercept of the Walden plot, respectively, for the Na[FSA][FTA][OTf]-PC system. The α parameters less than unity are observed below 2.5 m (0.84 for 2.5 m, 0.88 for 1.0 m, 0.99 for 0.5 m, and 0.96 for 0.1m), which is usual for such concentrated electrolytes or ionic liquids.[39, 43] The large α parameter for 5.0 m (1.13) may imply a highly decoupled transport phenomenon. Further systematic examination in a wide range of examples is required on this point. Smaller C' parameters than zero are interpreted by a poor dissociation of the ions in this temperature range; the Na[FSA][FTA][OTf]-PC systems are located below the diagonal dashed line in the Walden plot, indicating the strong interaction between ions.[39]

Cyclic voltammetry was conducted with an Al working electrode in the Na[FSA][FTA][OTf]-PC and single salts-PC samples at 5 mV s^{-1} (**Figure 2**). Na metal deposition/dissolution is observed during the cathodic scan. Al corrosion commences around 4 V vs. Na^{+}/Na during the anodic scan, as is typical among organic electrolytes containing fluorosulfonylamide anions. Aluminum corrosion suppressing effect is observed with increasing electrolyte concentrations and is completely attained in 5.0 m Na[FSA][FTA][OTf]-PC achieving a wide stability window of around 5 V (**Figure 2a**). This substantiates the merits of higher concentrations for improved oxidation stability. The same trend was observed in the single salt-PC samples. However, the single-salt could not suppress Al corrosion due to their low solubility compared to the ternary salt system with PC (**Figure 2b**).

The anodic limits for the Na[FSA][FTA][OTf] systems have been tested using a Pt electrode by the LSV measurements (**Figure S7**). The anodic limits of 0.1, 0.5, 1.0, 2.5, and 5.0 m

Na[FSA][FTA][OTf]-PC are obtained as 4.77, 4.84, 4.93, 4.98, and 5.33 V (threshold: 0.1 mA cm^{-2}), respectively. The LSV results reveal that the increase in the concentration of electrolytes improves oxidative stability.

The charge-discharge tests of HC and $NaCrO_2$ were conducted separately with a Na metal counter electrode **(Figure 3)**. An increase in concentration results in smaller polarization in both the Na/HC and Na/$NaCrO_2$ cells, providing improved charge-discharge capacities. The different concentration leads to dramatic performance changes in higher concentrations of the HC/Na cell. The first charge capacities are obtained to be only 137.6 mAh $(g\text{-}HC)^{-1}$ in 0.1 m Na[FSA][FTA][OTf]-PC, whereas more than twice capacity of 250.6 mAh $(g\text{-}HC)^{-1}$ is achieved in 5.0 m Na[FSA][FTA][OTf]-PC. The Coulombic efficiencies of the initial cycle are 46.1, 63.5, 65.6, and 66.8% as the order of increasing concentration of electrolytes, 0.1, 1.0, 2.5, and 5.0 m Na[FSA][FTA][OTf]-PC, respectively (Figure 3a). The Coulombic efficiencies of the initial cycle in the Na/$NaCrO_2$ show a similar trend that higher concentration results in slightly better efficiencies of 93.2, 95.6, 95.4, and 96.4 in 0.1, 1.0, 2.5, and 5.0 m Na[FSA][FTA][OTf]-PC, respectively (Figure 3b). However, this electrochemical performance is highly influenced by the stability and polarization of Na metal electrode against electrolytes. Therefore, Na metal deposition-dissolution behaviors were investigated with a Na metal symmetric cell.[45]

Na metal deposition-dissolution behavior was investigated in a Na metal symmetric cell with Na[FSA][FTA][OTf]-PC electrolytes at different concentrations (1.0 mA cm^{-2} for 1000 min (30 min per cycle)) **(Figure S8)**. The polarization profile confirms that 0.1 m Na[FSA][FTA][OTf]-PC has the largest polarization with the shortest cycling time compared to the cases at higher concentrations. The polarization decreases and cycling time improves with increasing concentration. These voltage profiles indicate that higher concentration leads to better

passivation ability toward Na metal, ultimately affecting the charge-discharge capacities and polarization in half-cell measurement. Moreover, the smaller polarization in a higher concentration is also observed with EIS using HC/HC and $NaCrO_2$/$NaCrO_2$ symmetric cells. (See the discussion below). The voltage profile of Na/Na with Na[FSA][FTA][OTf] (8:1:1) molten salts at 363 K shows the smallest polarization due to higher operational temperature. However, limited cycling life of this cell indicates faster electrolyte decomposition occurs at higher temperatures (**Figure S**9).

Electrochemical performance of the 5.0 m Na[FSA][FTA][OTf]-PC was further evaluated using a HC/$NaCrO_2$ full-cell at 298 K, where the capacity ratio of the positive and negative electrodes was set at HC / $NaCrO_2$ = 1.0 / 1.2 based on their practical capacities. The cell exhibited capacities of 263 mA $(g\text{-}HC)^{-1}$ and 77.1 mA $(g\text{-}NaCrO_2)^{-1}$ at 1C (= 125 mA g^{-1}) (**Figure 4a**). The d*Q*/d*V* curves indicate three redox reactions at 2.97, 3.01, and 3.07 V during charging and at 3.03, 2.99, and 2.93 V during discharging, associated with the Cr^{3+}/Cr^{4+} redox activity in $NaCrO_2$ (**Figure 4b**).[35] The cathodic and anodic peaks at 0.05 and 0.11V, respectively, indicate the reversible Na^+ insertion/extraction properties within HC.[46] Cycle performance tests of the $NaCrO_2$/HC cell indicated stable cyclability over 100 cycles at 1C. The Coulombic efficiency of the initial cycle and the average Coulombic efficiency over 100 cycles were 70.8 % (Figure S10) and 99.5 %, respectively. A remarkable full cell capacity retention of 86.9 % (vs. 1st-cycle capacity) was obtained after 100 cycles (**Figure 4c**).

Electrochemical impedance spectroscopy (EIS) was performed to investigate the kinetic characteristics with concentration effects. Symmetric cell configuration was adopted after adjusting the state of charge (SOC) to 30%. Because half-cell configuration could result in polarization based on a Na metal counter electrode, it is unsuitable for evaluating a targeted

electrode.[47-48] **Figure S11** shows the Nyquist plots and fitted curves of the HC/HC and $NaCrO_2$/$NaCrO_2$ symmetric cell. The equivalent circuit for fitting the Nyquist plots is depicted as the inset in Figure S11b, and the EIS parameters are provided in **Table S11**. According to the equivalent circuit, there are three different resistances of a bulk resistance (R_{bulk}), a resistance at the high-frequency region (R_1), and a resistance at the low-frequency region (R_2). R_{bulk} represents the resistance of the electrolyte, R_1 is related to the resistance between current collector/active material or SEI, and R_2 arises from charge-transfer resistance. The 0.1 m Na[FSA][FTA][OTf]-PC provides the smaller R_1 values (10.0 Ω for HC/HC and 17.4 Ω for $NaCrO_2$/$NaCrO_2$) than those of in 5.0 m Na[FSA][FTA][OTf]-PC (17.9 Ω for HC/HC and 21.8 Ω for $NaCrO_2$/$NaCrO_2$). This indicates a higher concentration causes a slightly higher resistance on this factor. On the contrary to R_1, the R_2 values of HC/HC and $NaCrO_2$/$NaCrO_2$ with 5.0 m Na[FSA][FTA][OTf]-PC (6661 Ω for HC/HC and 20.5 Ω for $NaCrO_2$/$NaCrO_2$) are significantly smaller than those with 0.1 m Na[FSA][FTA][OTf]-PC (13583 Ω for HC/HC and 25.6 Ω for $NaCrO_2$/$NaCrO_2$). When the full cell performance is considered, contributions of R_1 on the HC and $NaCrO_2$ electrodes and R_2 on the $NaCrO_2$ electrode are negligible because of the large contribution of R_2 on the HC electrode. Consequently, the EIS results emanate that the overall battery performance is ruled by the kinetics of the charge transfer process on the HC electrode (Figure S11a).

X-ray photoelectron spectroscopy was performed to further investigate the composition of the SEI layer on HC after the initial cycle in 0.1 m and 5.0 m Na[FSA][FTA][OTf]-PC. **Figure 5** shows Na 1s, F 1s, N 1s, S 2p, O 1s, and C1s XPS spectra of the HC electrode (see **Table S12** for further details of XPS peak assignments). The major SEI component of NaF from Na^+ and decomposed FSA^- is confirmed by the peaks at 1071.8 and 684.4 in the Na 1s and the F 1s spectra, respectively. The C-F and S-F peaks at 687.6 and 686.7 eV in the F 1s spectrum, respectively, are

more strongly observed with 5.0 m than those with 0.1 m Na[FSA][FTA][OTf]-PC. The C–N at 399.1 eV in N 1s and -SO_2- peak confirms at 169.3 eV in the S 2p should originate from the reduction of Na[FSA], Na[FTA], and Na[OTf].[12, 49] The characteristic peaks of the CF_2 group in PVDF are observed at 688.8 eV in the F 1s. The O 1s spectra confirm 0.1 m Na[FSA][FTA][OTf]-PC vividly has more C=O species than 5.0 m Na[FSA][FTA][OTf]-PC indicating SEI by the decomposition of PC because 0.1 m Na[FSA][FTA][OTf]-PC contains more free PC. A similar trend was observed in the peaks at 288.6 and 286.4 eV in the C 1s spectrums, referring to C=O and C-O bonds, respectively (Peaks at 283.2 eV is assigned to sodiated HC). These XPS results suggest that the components of SEI are similar in both the 0.1 m and 5.0 m Na[FSA][FTA][OTf]-PC, but the highly concentrated electrolyte contains more anion-derived SEI species. Reversely, more solvent-derived SEI species are found in the diluted electrolyte. These different interface properties can be understood based on the solution structure by Raman spectra, as illustrated in **Figure 6**.

The Raman spectra of PC, Na[FSA][FTA][OTf]-PC (0.1, 0.5, 1.0, 2.5, and 5.0 m) are shown in Figure 6a. The strong peak at 1783 cm^{-1} in the region of 1700-1900 cm^{-1} is assigned to the C=O stretching mode of PC. As the concentration increases, this peak exhibits a red-shift to 1793 cm^{-1} for 5.0 m Na[FSA][FTA][OTf]-PC, suggesting the interaction of the solvent and cation are increased.[50-51] The bending mode of the S-N-S group is found in the region of 680-780 cm^{-1}. The band at 712 cm^{-1} in the region of 680-780 cm^{-1} is assigned to the skeletal bending mode of the ring in pure PC[52-54] and shifts to the higher wavenumber with increasing electrolyte concentration. The three peaks observed in this region (724, 735, and 743 cm^{-1}) are attributed to the S-N-S bending mode of the FSA anion in the solvent-separated ion pair (SSIP), contact ion pair (CIP), and aggregates (AGG), respectively. The SSIP, CIP, and AGG contain an anion

interacting with the only solvent, with one Na^+ cation, and with more than two Na^+ cations (Figure 6b).[12, 55-56] The Raman spectra clearly indicate peak shifting from 724 to 743 cm^{-1} with increasing electrolyte concentration, suggesting that the CIP and AGG species increase at higher concentrations. Since the strong band of PC disturbs the fitting of SSIP, CIP, and AGG contribution in the band region of 722 to 743 cm^{-1}, their contribution is considered using another region of 1200-1240 cm^{-1} (the S=O stretching mode in FSA^-). According to previous work, three bands at 1216, 1220, and 1226 are assigned to SSIP, CIP, and AGG, respectively.[56] The band at 1228 cm^{-1} indicates the asymmetric stretching mode of the carbonate group in PC.[57] In the 0.1 m Na[FSA][FTA][OTf]-PC, the peaks are deconvoluted into the SSIP and solvent PC bands. Upon increasing the electrolyte concentration to 0.5 and 1.0 m Na[FSA][FTA][OTf]-PC, the CIP band increases because of the increased interaction between Na^+ and anion. As the electrolyte concentration reaches the 2.5 m Na[FSA][FTA][OTf]-PC, the band of PC disappeared, and the AGG peak appears, indicating all the solvent are coordinated, and anions are likely to coordinate with two or more Na^+. The same trend is shown in the single salt systems of 1.0 m and 2.5 m Na[FSA]-PC (**Figure S12**). In the case of 5.0 m Na[FSA][FTA][OTf]-PC, the contribution of the AGG band appears even more strongly while the SSIP band almost disappears comparing to 2.5 m Na[FSA]-PC and 2.5 m Na[FSA][FTA][OTf]-PC. Such Raman spectroscopic data demonstrate that the ternary salt system can achieve high concentration with a unique solution structure mainly composed of the AGG and CIP. The Raman spectra and XPS results demonstrate that the solvent- and anion-based SEI formation mechanisms of solvent- and anion-based in the diluted and concentrated electrolytes, respectively, which follows interface properties established in the concentrated electrolyte in Li-ion batteries studies (Figure 6b).[55]

4. CONCLUSION

In summary, the use of the ternary molten salt system was beneficial to explore highly concentrated electrolytes for Na-ion batteries. The Na[FSA][FTA][OTf] system (8 : 1 : 1 in mol) achieved high solubilities into various organic solvents, and the highest concentration of 5.0 m in the knows Na-based organic electrolytes was achieved with PC. Ionic conductivity of the Na[FSA][FTA][OTf]-PC electrolyte exhibits a maximum at 1.0 m, holding the fractional Walden rule between molar ionic conductivity and viscosity. Cyclic voltammetry showed the onset of Al corrosion around 4 V vs. Na^+/Na, which was caused in the presence of fluorosulfonylamide anion in the low-concentration Na[FSA][FTA][OTf]-PC electrolyte. On the other hand, the 5.0 m Na[FSA][FTA][OTf]-PC provides a wide electrochemical window, suppressing the Al corrosion issues. The excellent electrochemical performance was achieved with 5.0 m Na[FSA][FTA][OTf]-PC using a HC/$NaCrO_2$ full-cell at 298 K; the discharge capacities of 263 mAh $(g\text{-}HC)^{-1}$ and 77.1 mAh $(g\text{-}NaCrO_2)^{-1}$ were achieved at 1C (= 125 mA g^{-1}). In addition to this, stable cycleability over 100 cycles at 1C was confirmed from a cycle performance test of the full cell. In terms of coulombic efficiency, 70.8 % was achieved during the initial cycle, whereas 99.5 % was achieved as an average over 100 cycles. Remarkable full cell capacity retention of 86.9 % (vs. 1st-cycle capacity) was also achieved at the 100th cycle.

The highly concentrated electrolyte promoted the increasing amount of the CIP and AGG species, leading to the formation of a robust SEI layer, and achieved improvement in electrochemical performance. These results imply the use of the ternary molten salt systems as a propitious approach not only to the exploration of highly concentrated nonaqueous electrolytes but also aqueous and other nonaqueous systems for secondary batteries.

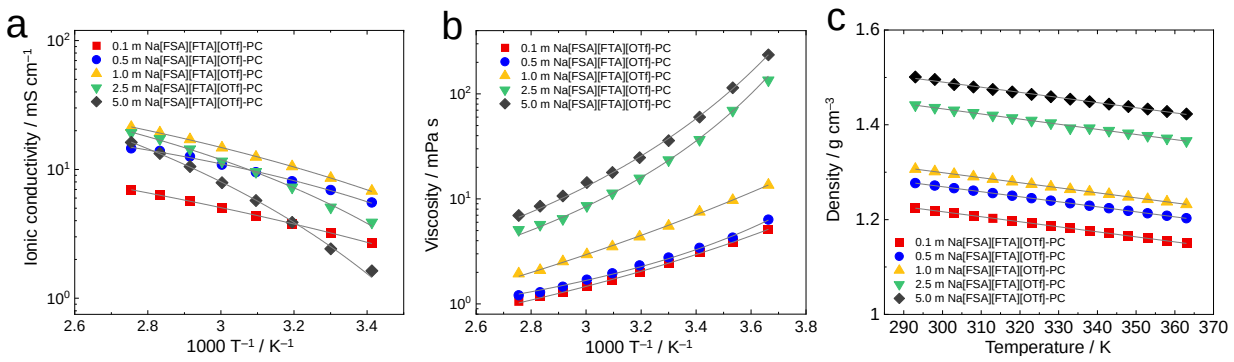

Figure 1. Temperature dependence of (a) ionic conductivities, (b) viscosities, and (c) densities for the Na[FSA][FTA][OTf]-PC systems.

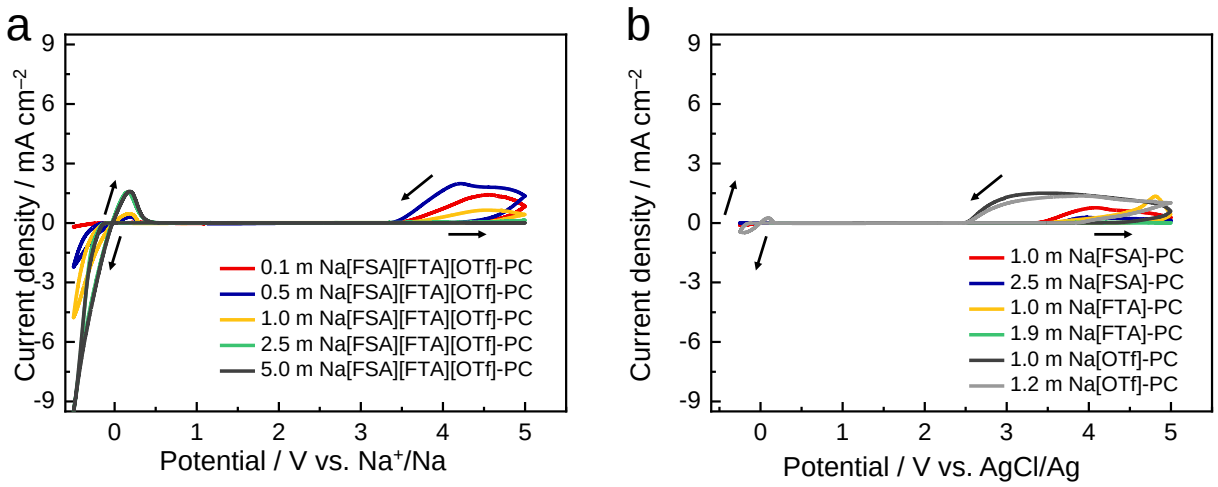

Figure 2. Cyclic voltammograms of the Al electrode at 5 mV s^{-1} with (a) the Na[FSA][FTA][OTf]-PC systems and (b) the single salt-PC systems.

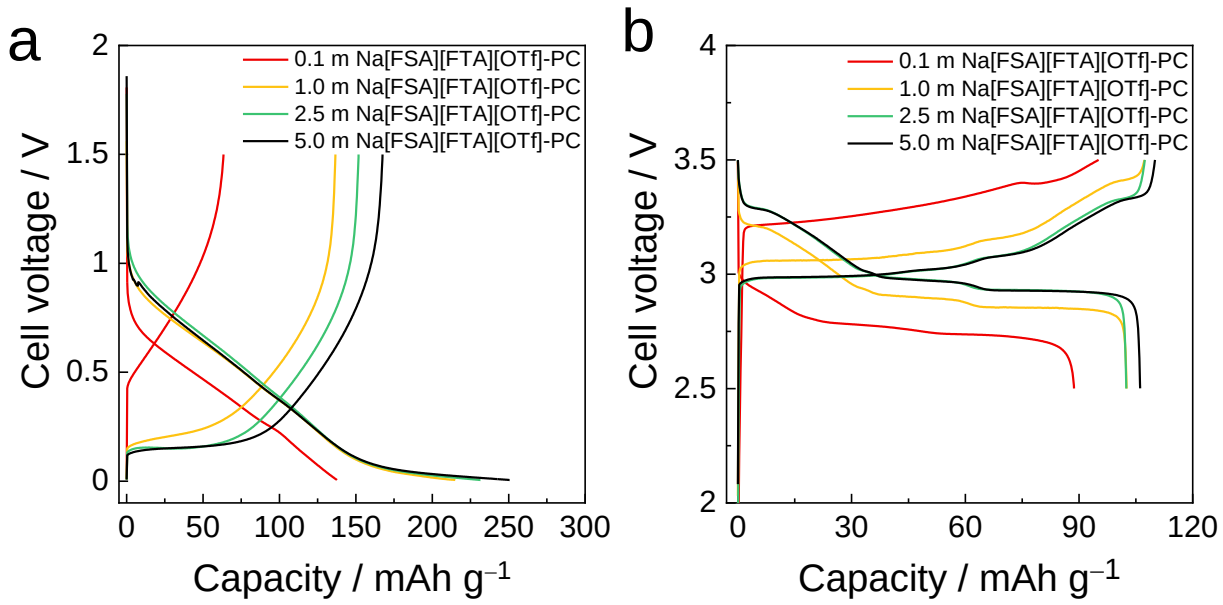

Figure 3. Charge-discharge curves of (a) the Na/HC cell with the cutoff voltages of 0.005–1.5 V and (b) the Na/$NaCrO_2$ cell with the cutoff voltages of 2.5–3.5 V. Temperature: 298 K and current density: 125 mA g^{-1}

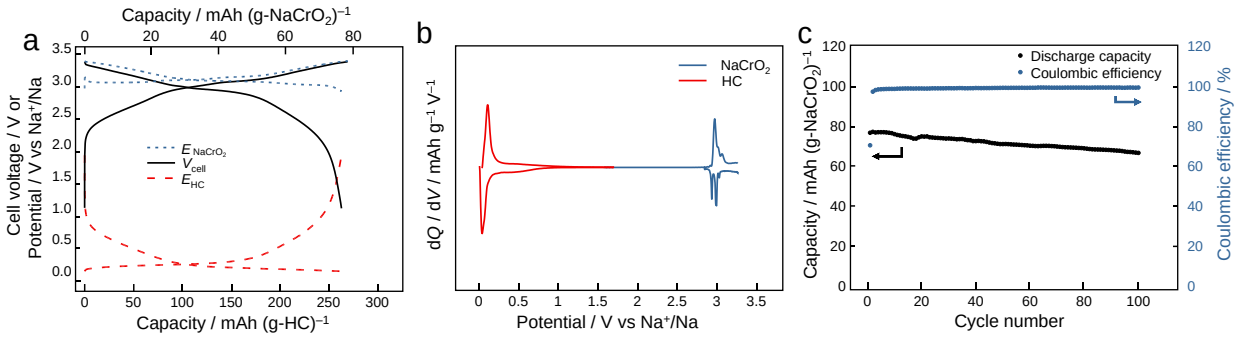

Figure 4. Results of electrochemical measurements conducted on the Na[FSA][FTA][OTf]-PC systems. (a) charge-discharge curves (the second cycle is plotted, See Figure S10, Supporting Information for the initial cycle) of the HC/$NaCrO_2$ cell using 5.0 m Na[FSA][FTA][OTf]-PC at 125 mA g^{-1}, (b) d*Q*/d*V* plots derived from the charge-discharge curves in (a), and (c) cycle performance of the HC/$NaCrO_2$ using the 5.0 m Na[FSA][FTA][OTf]-PC at 125 mA g^{-1}.

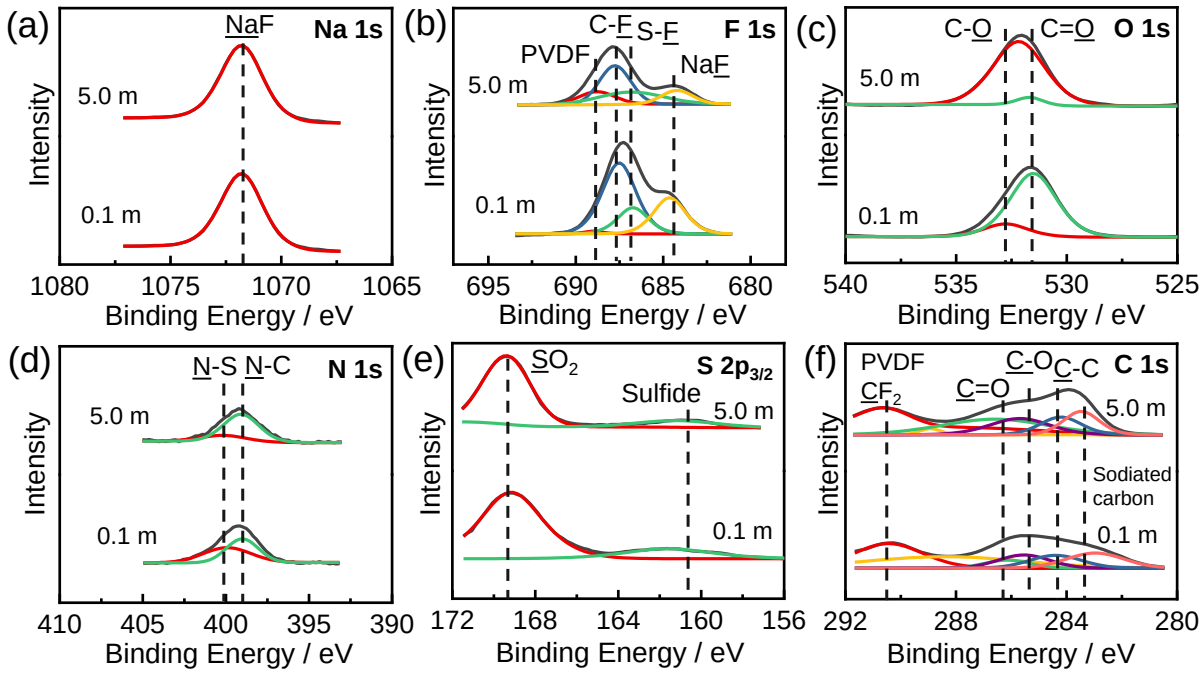

Figure 5. XPS spectra of the HC electrode in the HC/$NaCrO_2$ cell after the first cycle. 0.1 m and 5.0 m refer to the 0.1 m Na[FSA][FTA][OTf]-PC and 5.0 m Na[FSA][FTA][OTf]-PC systems, respectively. (a) Na 1s, (b) F 1s, (c) O 1s, (d) N 1s, (e) S 2p, and (f) C 1s regions. (See Table S12, Supporting Information for the SEI components and binding energy for the XPS peaks)

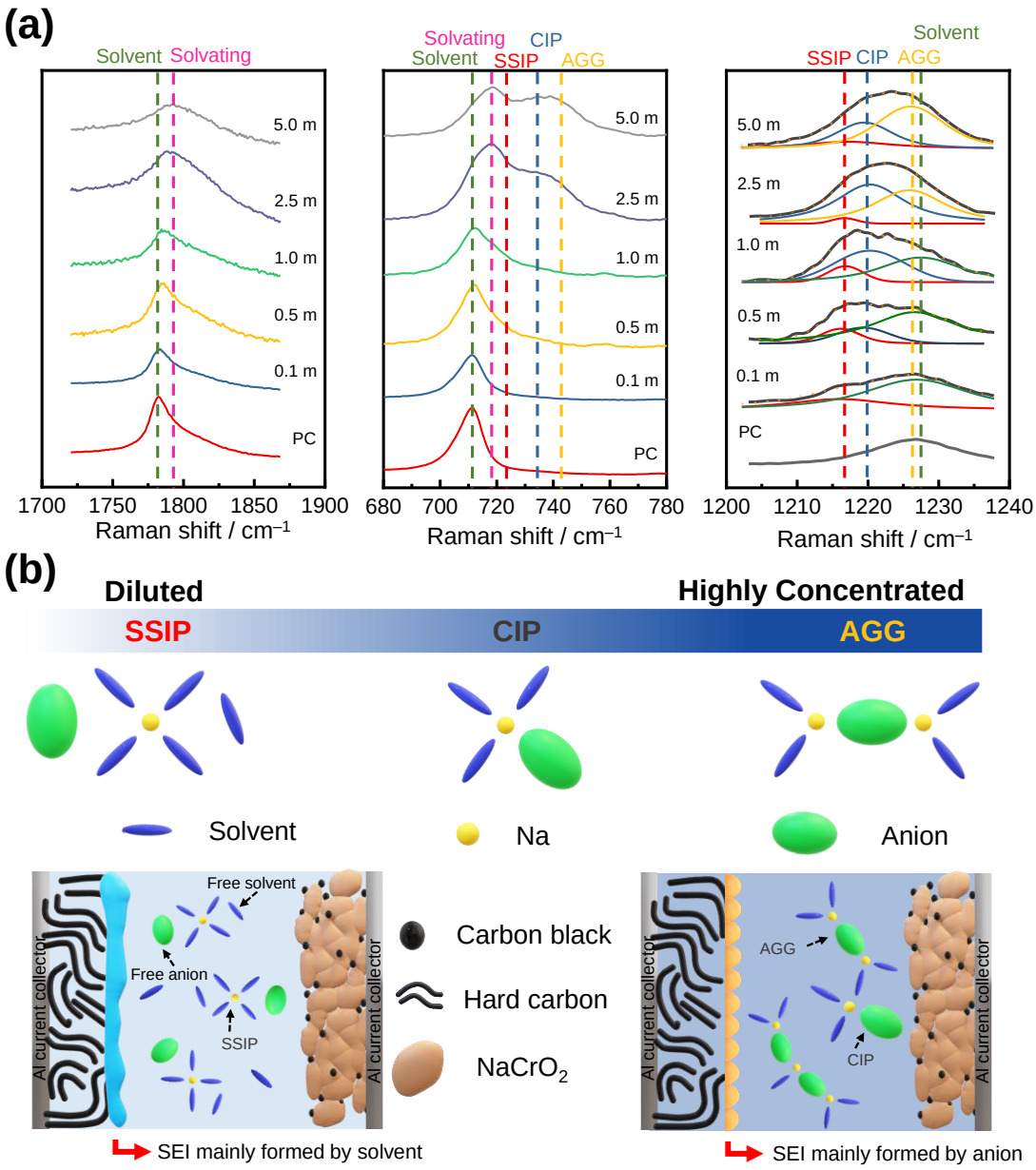

Figure 6. (a) Raman spectra and fitting curves of PC solvent, and the Na[FSA][FTA][OTf]-PC. 0.1, 0.5, 1.0, 2.5, and 5.0 m refer to the 0.1, 0.5, 1.0, 2.5, and 5.0 m Na[FSA][FTA][OTf]-PC systems, respectively. Organge dotted lines indicate cumulative fit. (b) Schematic illustration of Na^+ solvate species (solvent-separated ion pairs (SSIP), contacted ion pair (CIP) aggregate, (AGG)) and different the HC/electrolyte interface by salt concentration in electrolytes.

ASSOCIATED CONTENT

Supporting Information.

The Supporting Information is available free of charge at DOI: xx.

Experimental section, ionic conductivities, viscosities, cyclic voltammetry curves, and DSC data (PDF)

AUTHOR INFORMATION

Corresponding Author

*Phone: +81 75 753 5827. Fax: +81 75 753 5906. E-mail: k-matsumoto@energy.kyoto-u.ac.jp (K.M.).

ORCID

Jinkwang Hwang: 0000-0003-4800-3158

Huan Yang: 0000-0002-8757-5733

Kazuhiko Matsumoto: 0000-0002-0770-9210

Rika Hagiwara: 0000-0002-7234-3980

Notes

The authors declare no competing financial interest.

ACKNOWLEDGMENT

This study was supported by the Japanese Ministry of Education, Culture, Sports, Science and Technology (MEXT) program "Elements Strategy Initiative to Form Core Research Center" (JPMXP0112101003).

5. REFERENCES

(1) Cano, Z. P.; Banham, D.; Ye, S.; Hintennach, A.; Lu, J.; Fowler, M.; Chen, Z. Batteries and Fuel Cells for Emerging Electric Vehicle Markets. *Nat. Energy* **2018,** *3*, 279-289.

(2) Larcher, D.; Tarascon, J. M. Towards Greener and More Sustainable Batteries for Electrical Energy Storage. *Nat. Chem.* **2015,** *7*, 19-29.

(3) Huang, Y.; Zhao, L.; Li, L.; Xie, M.; Wu, F.; Chen, R. Electrolytes and Electrolyte/Electrode Interfaces in Sodium-Ion Batteries: From Scientific Research to Practical Application. *Adv. Mater.* **2019,** *31*, 1808393.

(4) Darling, R. M.; Gallagher, K. G.; Kowalski, J. A.; Ha, S.; Brushett, F. R. Pathways to Low-Cost Electrochemical Energy Storage: A Comparison of Aqueous and Nonaqueous Flow Batteries. *Energy Environ. Sci.* **2014,** *7*, 3459-3477.

(5) Kim, S.-W.; Seo, D.-H.; Ma, X.; Ceder, G.; Kang, K. Electrode Materials for Rechargeable Sodium-Ion Batteries: Potential Alternatives to Current Lithium-Ion Batteries. *Adv. Energy Mater.* **2012,** *2*, 710-721.

(6) Deng, J.; Luo, W.-B.; Chou, S.-L.; Liu, H.-K.; Dou, S.-X. Sodium-Ion Batteries: From Academic Research to Practical Commercialization. *Adv. Energy Mater.* **2018,** *8*, 1701428.

(7) Delmas, C. Sodium and Sodium-Ion Batteries: 50 Years of Research. *Adv. Energy Mater*. **2018,** *8*, 1703137.

(8) Hwang, J. Y.; Myung, S. T.; Sun, Y. K. Sodium-Ion Batteries: Present and Future. *Chem. Soc. Rev.* **2017,** *46*, 3529-3614.

(9) Ponrouch, A.; Monti, D.; Boschin, A.; Steen, B.; Johansson, P.; Palacín, M. R. Non-Aqueous Electrolytes for Sodium-Ion Batteries. *J. Mater. Chem. A* **2015,** *3*, 22-42.

(10) Mogensen, R.; Brandell, D.; Younesi, R. Solubility of the Solid Electrolyte Interphase (Sei) in Sodium Ion Batteries. *ACS Energy Lett.* **2016,** *1*, 1173-1178.

(11) Matsumoto, K.; Hwang, J.; Kaushik, S.; Chen, C.-Y.; Hagiwara, R. Advances in Sodium Secondary Batteries Utilizing Ionic Liquid Electrolytes. *Energy Environ. Sci.* **2019,** *12*, 3247-3287.

(12) Takada, K.; Yamada, Y.; Watanabe, E.; Wang, J.; Sodeyama, K.; Tateyama, Y.; Hirata, K.; Kawase, T.; Yamada, A. Unusual Passivation Ability of Superconcentrated Electrolytes toward Hard Carbon Negative Electrodes in Sodium-Ion Batteries. *ACS Appl. Mater. Interfaces* **2017,** *9*, 33802-33809.

(13) Åvall, G.; Mindemark, J.; Brandell, D.; Johansson, P. Sodium-Ion Battery Electrolytes: Modeling and Simulations. *Adv. Energy Mater.* **2018,** *8*, 1703036.

(14) Li, M.; Wang, C.; Chen, Z.; Xu, K.; Lu, J. New Concepts in Electrolytes. *Chem. Rev.* **2020,** *120*, 6783-6819.

(15) Suo, L.; Borodin, O.; Gao, T.; Olguin, M.; Ho, J.; Fan, X.; Luo, C.; Wang, C.; Xu, K. "Water-in-Salt" Electrolyte Enables High-Voltage Aqueous Lithium-Ion Chemistries. *Science* **2015,** *350*, 938-943.

(16) Chen, L.; Zhang, J.; Li, Q.; Vatamanu, J.; Ji, X.; Pollard, T. P.; Cui, C.; Hou, S.; Chen, J.; Yang, C.; Ma, L.; Ding, M. S.; Garaga, M.; Greenbaum, S.; Lee, H.-S.; Borodin, O.; Xu, K.; Wang, C. A 63 M Superconcentrated Aqueous Electrolyte for High-Energy Li-Ion Batteries. *ACS Energy Lett.* **2020,** *5*, 968-974.

(17) Zhang, H.; Qin, B.; Han, J.; Passerini, S. Aqueous/Nonaqueous Hybrid Electrolyte for Sodium-Ion Batteries. *ACS Energy Lett.* **2018,** *3*, 1769-1770.

(18) Yamada, Y.; Furukawa, K.; Sodeyama, K.; Kikuchi, K.; Yaegashi, M.; Tateyama, Y.; Yamada, A. Unusual Stability of Acetonitrile-Based Superconcentrated Electrolytes for Fast-Charging Lithium-Ion Batteries. *J. Am. Chem. Soc.* **2014,** *136*, 5039-5046.

(19) Kühnel, R.-S.; Reber, D.; Battaglia, C. A High-Voltage Aqueous Electrolyte for Sodium-Ion Batteries. *ACS Energy Lett.* **2017,** *2*, 2005-2006.

(20) Wang, J.; Yamada, Y.; Sodeyama, K.; Chiang, C. H.; Tateyama, Y.; Yamada, A. Superconcentrated Electrolytes for a High-Voltage Lithium-Ion Battery. *Nat. Commun.* **2016,** *7*, 12032.

(21) Ko, S.; Yamada, Y.; Yamada, A. A 62 m K-Ion Aqueous Electrolyte. *Electrochem. Commun.* **2020,** *116*, 106764.

(22) Yamada, Y.; Usui, K.; Sodeyama, K.; Ko, S.; Tateyama, Y.; Yamada, A. Hydrate-Melt Electrolytes for High-Energy-Density Aqueous Batteries. *Nat. Energy* **2016,** *1*, 16129.

(23) Suo, L.; Borodin, O.; Sun, W.; Fan, X.; Yang, C.; Wang, F.; Gao, T.; Ma, Z.; Schroeder, M.; von Cresce, A.; Russell, S. M.; Armand, M.; Angell, A.; Xu, K.; Wang, C. Advanced High-Voltage Aqueous Lithium-Ion Battery Enabled by "Water-in-Bisalt" Electrolyte. *Angew. Chem., Int. Ed.* **2016,** *55*, 7136-7141.

(24) Jiang, L.; Liu, L.; Yue, J.; Zhang, Q.; Zhou, A.; Borodin, O.; Suo, L.; Li, H.; Chen, L.; Xu, K.; Hu, Y.-S. High-Voltage Aqueous Na-Ion Battery Enabled by Inert-Cation-Assisted Water-in-Salt Electrolyte. *Adv. Mater.* **2020,** *32*, 1904427.

(25) Yue, J.; Lin, L.; Jiang, L.; Zhang, Q.; Tong, Y.; Suo, L.; Hu, Y.-s.; Li, H.; Huang, X.; Chen, L. Interface Concentrated-Confinement Suppressing Cathode Dissolution in Water-in-Salt Electrolyte. *Adv. Energy Mater.* **2020,** 10, 2000665.

(26) Reber, D.; Kühnel, R.-S.; Battaglia, C. Suppressing Crystallization of Water-in-Salt Electrolytes by Asymmetric Anions Enables Low-Temperature Operation of High-Voltage Aqueous Batteries. *ACS Materials Lett.* **2019,** *1*, 44-51.

(27) Okoshi, M.; Chou, C.-P.; Nakai, H. Theoretical Analysis of Carrier Ion Diffusion in Superconcentrated Electrolyte Solutions for Sodium-Ion Batteries. *J. Phys. Chem. C* **2018,** *122*, 2600-2609.

(28) Lee, M. H.; Kim, S. J.; Chang, D.; Kim, J.; Moon, S.; Oh, K.; Park, K.-Y.; Seong, W. M.; Park, H.; Kwon, G.; Lee, B.; Kang, K. Toward a Low-Cost High-Voltage Sodium Aqueous Rechargeable Battery. *Mater. Today* **2019,** *29*, 26-36.

(29) Zhang, H.; Jeong, S.; Qin, B.; Vieira Carvalho, D.; Buchholz, D.; Passerini, S. Towards High-Performance Aqueous Sodium-Ion Batteries: Stabilizing the Solid/Liquid Interface for Nasicon-Type Na2vti(Po4)3 Using Concentrated Electrolytes. *ChemSusChem* **2018,** *11*, 1382-1389.

(30) Lee, J.; Lee, Y.; Lee, J.; Lee, S.-M.; Choi, J.-H.; Kim, H.; Kwon, M.-S.; Kang, K.; Lee, K. T.; Choi, N.-S. Ultraconcentrated Sodium Bis(Fluorosulfonyl)Imide-Based Electrolytes for High-Performance Sodium Metal Batteries. *ACS Appl. Mater. Interfaces* **2017,** *9*, 3723-3732.

(31) Ferdousi, S. A.; Hilder, M.; Basile, A.; Zhu, H.; O'Dell, L. A.; Saurel, D.; Rojo, T.; Armand, M.; Forsyth, M.; Howlett, P. C. Water as an Effective Additive for High-Energy-Density Na Metal Batteries? Studies in a Superconcentrated Ionic Liquid Electrolyte. *ChemSusChem* **2019,** *12*, 1700-1711.

(32) Suo, L.; Borodin, O.; Wang, Y.; Rong, X.; Sun, W.; Fan, X.; Xu, S.; Schroeder, M. A.; Cresce, A. V.; Wang, F.; Yang, C.; Hu, Y.-S.; Xu, K.; Wang, C. "Water-in-Salt" Electrolyte Makes Aqueous Sodium-Ion Battery Safe, Green, and Long-Lasting. *Adv. Energy Mater.* **2017,** *7*, 1701189.

(33) Braconnier, J. J.; Delmas, C.; Hagenmuller, P. Etude Par Desintercalation Electrochimique Des Systemes Naxcro2 Et Naxnio2. *Mater. Res. Bull.* **1982,** *17*, 993-1000.

(34) Komaba, S.; Yabuuchi, N.; Nakayama, T.; Ogata, A.; Ishikawa, T.; Nakai, I. Study on the Reversible Electrode Reaction of Na1–Xni0.5mn0.5o2 for a Rechargeable Sodium-Ion Battery. *Inorg. Chem.* **2012,** *51*, 6211-6220.

(35) Yu, C.-Y.; Park, J.-S.; Jung, H.-G.; Chung, K.-Y.; Aurbach, D.; Sun, Y.-K.; Myung, S.-T. Nacro2 Cathode for High-Rate Sodium-Ion Batteries. *Energy Environ. Sci.* **2015,** *8*, 2019-2026.

(36) Xia, X.; Dahn, J. R. Nacro2 Is a Fundamentally Safe Positive Electrode Material for Sodium-Ion Batteries with Liquid Electrolytes. *Electrochem. Solid-State Lett.* **2012,** *15*, A1.

(37) Chen, C.-Y.; Matsumoto, K.; Nohira, T.; Hagiwara, R.; Fukunaga, A.; Sakai, S.; Nitta, K.; Inazawa, S. Electrochemical and Structural Investigation of Nacro2 as a Positive Electrode for Sodium Secondary Battery Using Inorganic Ionic Liquid Nafsa–Kfsa. *J. Power Sources* **2013,** *237*, 52-57.

(38) Matsumoto, K.; Taniki, R.; Nohira, T.; Hagiwara, R. Inorganic-Organic Hybrid Ionic Liquid Electrolytes for Na Secondary Batteries. *J. Electrochem. Soc.* **2015,** *162*, A1409-A1414.

(39) Xu, W.; Cooper, E. I.; Angell, C. A. Ionic Liquids: Ion Mobilities, Glass Temperatures, and Fragilities. *J. Phys. Chem. C* **2003,** *107*, 6170-6178.

(40) Francke, R.; Cericola, D.; Kötz, R.; Weingarth, D.; Waldvogel, S. R. Novel Electrolytes for Electrochemical Double Layer Capacitors Based on 1,1,1,3,3,3-Hexafluoropropan-2-Ol. *Electrochim. Acta* **2012,** *62*, 372-380.

(41) Izutsu, K. *Electrochemistry in Nonaqueous Solutions, 2nd, Revised and Enlarged Edition*, Wiley-VCH: Weinheim, 2009.

(42) Yoon, H.; Best, A. S.; Forsyth, M.; MacFarlane, D. R.; Howlett, P. C. Physical Properties of High Li-Ion Content N-Propyl-N-Methylpyrrolidinium Bis(Fluorosulfonyl)Imide Based Ionic Liquid Electrolytes. *Phys. Chem. Chem. Phys.* **2015,** *17*, 4656-4663.

(43) Westman, K.; Dugas, R.; Jankowski, P.; Wieczorek, W.; Gachot, G.; Morcrette, M.; Irisarri, E.; Ponrouch, A.; Palacin, M. R.; Tarascon, J. M.; Johansson, P. Diglyme Based Electrolytes for Sodium-Ion Batteries. *ACS Appl. Energy Mater.* **2018,** *1*, 2671-2680.

(44) Matsumoto, K.; Okamoto, Y.; Nohira, T.; Hagiwara, R. Thermal and Transport Properties of Na[N(So2f)2]–[N-Methyl-N-Propylpyrrolidinium][N(So2f)2] Ionic Liquids for Na Secondary Batteries. *J. Phys. Chem. C* **2015,** *119*, 7648-7655.

(45) Hwang, J.; Takeuchi, K.; Matsumoto, K.; Hagiwara, R. Nasicon Vs. Na Metal: A New Counter Electrode to Evaluate Electrodes for Na Secondary Batteries. *J. Mater. Chem. A* **2019,** *7*, 27057-27065.

(46) Komaba, S.; Murata, W.; Ishikawa, T.; Yabuuchi, N.; Ozeki, T.; Nakayama, T.; Ogata, A.; Gotoh, K.; Fujiwara, K. Electrochemical Na Insertion and Solid Electrolyte Interphase for Hard-Carbon Electrodes and Application to Na-Ion Batteries. *Adv. Funct. Mater.* **2011,** *21*, 3859-3867.

(47) Hwang, J.; Matsumoto, K.; Hagiwara, R. Symmetric Cell Electrochemical Impedance Spectroscopy of Na2fep2o7 Positive Electrode Material in Ionic Liquid Electrolytes. *J. Phys. Chem. C* **2018,** *122*, 26857-26864.

(48) Hwang, J.; Matsumoto, K.; Hagiwara, R. Electrolytes toward High-Voltage Na3v2(Po4)2f3 Positive Electrode Durable against Temperature Variation. *Adv. Energy Mater.* **2020,** *10*, 2001880.

(49) Patra, J.; Huang, H.-T.; Xue, W.; Wang, C.; Helal, A. S.; Li, J.; Chang, J.-K. Moderately Concentrated Electrolyte Improves Solid–Electrolyte Interphase and Sodium Storage Performance of Hard Carbon. *Energy Storage Mater.* **2019,** *16*, 146-154.

(50) Giorgini, M. G.; Futamatagawa, K.; Torii, H.; Musso, M.; Cerini, S. Solvation Structure around the Li+ Ion in Mixed Cyclic/Linear Carbonate Solutions Unveiled by the Raman Noncoincidence Effect. *J. Phys. Chem. Lett.* **2015,** *6*, 3296-3302.

(51) Konefał, R.; Morávková, Z.; Paruzel, B.; Patsula, V.; Abbrent, S.; Szutkowski, K.; Jurga, S. Effect of Pamam Dendrimers on Interactions and Transport of Litfsi and Natfsi in Propylene Carbonate-Based Electrolytes. *Polymers* **2020,** *12*, 1595.

(52) Chang, Z.-h.; Wang, J.-t.; Wu, Z.-h.; Gao, M.; Wu, S.-j.; Lu, S.-g. The Electrochemical Performance of Silicon Nanoparticles in Concentrated Electrolyte. *ChemSusChem* **2018,** *11*, 1787-1796.

(53) Kondo, K.; Sano, M.; Hiwara, A.; Omi, T.; Fujita, M.; Kuwae, A.; Iida, M.; Mogi, K.; Yokoyama, H. Conductivity and Solvation of Li+ Ions of Lipf6 in Propylene Carbonate Solutions. *J. Phys. Chem. C* **2000,** *104*, 5040-5044.

(54) Doi, T.; Masuhara, R.; Hashinokuchi, M.; Shimizu, Y.; Inaba, M. Concentrated Lipf6/Pc Electrolyte Solutions for 5-V Lini0.5mn1.5o4 Positive Electrode in Lithium-Ion Batteries. *Electrochim. Acta* **2016,** *209*, 219-224.

(55) Yamada, Y.; Yaegashi, M.; Abe, T.; Yamada, A. A Superconcentrated Ether Electrolyte for Fast-Charging Li-Ion Batteries. *Chem. Commun.* **2013,** *49*, 11194-11196.

(56) Shi, P.; Zheng, H.; Liang, X.; Sun, Y.; Cheng, S.; Chen, C.; Xiang, H. A Highly Concentrated Phosphate-Based Electrolyte for High-Safety Rechargeable Lithium Batteries. *Chem. Commun.* **2018,** *54*, 4453-4456.

(57) Janz, G. J.; Ambrose, J.; Coutts, J. W.; Downey, J. R. Raman Spectrum of Propylene Carbonate. *Spectrochim. Acta A Mol. Biomol. Spectrosc.* **1979,** *35*, 175-179.

TOC GRAPHICS